Nanoscale

PAPER

View Article Online
View Journal | View Issue

Cite this: *Nanoscale*, 2026, **18**, 328

Distribution of oxygen vacancies and their impact on the charge state of Pt on TiO_2

Ryugen Suzuki,[a] Hisahiro Einaga [b] and Hajime Hojo *[b]

Received 12th July 2025,
Accepted 25th November 2025

DOI: 10.1039/d5nr02953h

rsc.li/nanoscale

It is well known that interactions between the support and metal particles, called metal–support interactions, considerably affect the activity of supported metal catalysts. Two representative consequences of these interactions are the formation of lattice defects at the metal–support perimeter and the change in the charge state of metal particles. However, the identification of control parameters for tuning metal–support interactions is not simple because many factors can affect metal–support interactions. Herein, a model Pt/TiO_2 catalyst based on an epitaxial TiO_2 thin film was developed and the distribution of oxygen defects and the charge state of Pt on this catalyst were investigated using scanning transmission electron microscopy, electron energy loss spectroscopy, X-ray photoelectron spectroscopy, and first-principles calculations. Results showed that oxygen vacancies are easily formed just below Pt nanoparticles. Moreover, it was revealed that Pt nanoparticles supported on TiO_2 (101) are negatively charged. Oxygen vacancies promote charge transfer to Pt nanoparticles, and Pt becomes more negatively charged than that on stoichiometric TiO_2. This study demonstrates that the charge state of Pt is affected by the presence of oxygen vacancies on the support, providing an important guideline for controlling metal–support interactions to develop catalysts with desired properties.

Introduction

Supported metal catalysts are widely used to facilitate various chemical reactions. Increasing the selectivity and activity of such catalysts has been the central focus of catalytic research to realize the efficient utilization of precious metals. Not only the metal nanoparticles, but also the support often affect the catalytic properties of supported metal catalysts *via* interactions called metal–support interactions.[1–3] It is well accepted that the active sites on most supported metal catalysts are the periphery sites of the nanoparticles and support.[4,5] In this regard, one of the critical interactions is to promote the formation of oxygen vacancies at the metal–oxide interface because reducibility is an essential characteristic of oxide catalysts in oxidation reaction following the Mars–van Krevelen mechanism,[6] in which lattice oxygen is used for the reaction. Indeed, it has been experimentally and theoretically demonstrated that the formation of oxygen vacancies at periphery sites is typically a key step in the CO oxidation and/or water gas shift reactions of Au/TiO_2 [7–11] and Pt/TiO_2 [12–16] catalysts.

Furthermore, the presence of oxygen vacancies at the metal–oxide interface can change the charge state of metal nanoparticles,[17,18] which is a critical factor affecting the catalytic properties of these catalysts.[19–22] This is because in the framework of solid-state physics, the direction and amount of charge transfer between two materials are generally explained by the difference in their work functions,[17] and the presence of oxygen vacancies decreases the work functions of oxides.[23] Such an electronic interaction between the metal nanoparticles and support is called the electronic metal–support interaction,[20] constituting one of the important categories of metal–support interactions.

Therefore, the oxygen vacancies on the support considerably affect the catalytic properties of supported metal catalysts. Among reducible oxides, TiO_2 has been one of the most widely employed supports because it is inexpensive, thermally and chemically stable, and its oxygen vacancy concentration can be tuned controllably by thermal reduction treatments. Moreover, rutile-type TiO_2 offers single-crystal substrates with well-defined surfaces, including (110), (001), and (100),[24] enabling systematic investigations of surface structure effects. Pt/TiO_2 catalysts, in particular, have been widely studied not only for conventional heterogenous catalysis but also for electrocatalytic reactions such as the oxygen reduction reaction and hydrogen evolution reaction,[25–27] as well as photocatalytic processes.[28] These diverse applications highlight the importance of understanding and controlling metal–support interactions in Pt/TiO_2 systems. However, the distribution of oxygen vacancies on the support remains poorly understood because

[a]*Graduate School of Engineering Sciences, Kyushu University, 816-8580, Japan*
[b]*Faculty of Engineering Sciences, Kyushu University, 816-8580, Japan.*
E-mail: hojo.hajime.100@m.kyushu-u.ac.jp

of difficulties in directly observing them in real space. Furthermore, many previous studies have focused on practical catalysts with indefinite structures, and little is known about the parameters controlling metal–support interactions. Assuming that the nature of metal–support interactions can vary depending on the crystalline surfaces and stoichiometries of supports, it is necessary to study their nature using model catalysts with well-defined surfaces. In this context, numerous studies have used the surface science approach.[29] Because scanning tunneling microscopy is generally used in such studies, samples must be sufficiently conductive. When constructing model supported metal catalysts with oxide supports, ultrathin films of oxides on conducting single-crystal metal substrates are typically used.[30] However, ultrathin films can be deformed due to epitaxial strain and controlling the stoichiometry of these films is not easy, especially for transition metal oxides. The single crystals of TiO_2 have often been used because they can be imparted conductivity *via* annealing treatment in a vacuum by introducing oxygen vacancies.[31–35] That is, such TiO_2 single crystals are nonstoichiometric. Indeed, in our previous study, we demonstrated that Pt nanoparticles on TiO_2 (110) can be either positively or negatively charged using ultrahigh sensitive and precision electron holography and the stoichiometry of TiO_2 is one of the key factors determining the charge state of Pt nanoparticles.[17]

Herein, epitaxial thin film-based model catalysts were developed to study the interaction between Pt nanoparticles and stoichiometric TiO_2 with arbitrary and unstable lattice planes such as the (101) plane.[36,37] In the field of surface science, it has been reported that when Pt is deposited on TiO_2 (110) with oxygen vacancies, the Ti^{3+} component disappears due to charge transfer from Ti^{3+} to Pt,[38] although no noticeable shift in the Pt binding energy was observed; similar behavior has also been reported for oxygen-deficient $SrTiO_3$(111).[39] Building on these findings, the present study uniquely clarifies how the spatial distribution of oxygen vacancies influences the electronic state of Pt on rutile-type TiO_2 (101) by combining scanning transmission electron microscopy (STEM), electron energy-loss spectroscopy (EELS), X-ray photoelectron spectroscopy (XPS), and first-principles calculations based on density functional theory (DFT).

Experimental

Preparation of Pt/TiO_2 model catalysts

A TiO_2 thin-film support was prepared *via* pulsed laser deposition. TiO_2 targets were made of a rutile TiO_2 powder with 99.99% purity. Thin films were grown on *r*-plane α-Al_2O_3 substrates at a substrate temperature of 700 °C under an oxygen pressure of 1.0 Pa by focusing a Nd:YAG laser (λ = 266 nm, 2.0 J cm^{-2}, 10 Hz) on the TiO_2 target.[18,40] The specimens for cross-sectional STEM observations were prepared *via* focused ion beam (Thermo Fisher Scientific (TFS) Inc., Scios). The specimens for plan-view STEM observations were prepared *via* back thinning from the substrate side, which included mechanical polishing, dimple grinding, and Ar ion milling. Pt nanoparticles were loaded onto plan-view TEM samples for STEM observations and onto as-deposited TiO_2 films for XPS measurements *via* the photodeposition method. The TEM sample was immersed into an ethanol (1 mL)–water (9 mL) solution containing 5.8×10^{-9} mol of $H_2PtCl_6{\cdot}6H_2O$ in a Pyrex glass vessel. For the TiO_2 thin film samples used in XPS measurements, the amount of $H_2PtCl_6{\cdot}6H_2O$ was adjusted according to the surface area of each sample. The sample and solution were then photoirradiated using a 500 W high-pressure Hg lamp for 3 h with continuous stirring. For postdeposition treatment, the sample was heated in air at 673 K for 2 h and then in an H_2 flow at 473 K for 1 h to ensure direct contact between the nanoparticles and support.[41]

Characterization

The crystal structures of films were investigated *via* X-ray diffraction (XRD) with Cu Kα radiation (Rigaku, SmartLab SE). The surface morphologies of films were observed *via* atomic force microscopy (AFM; Agilent 5500). Raman spectra were measured with a Nanofinder 30 (Tokyo Instruments) using a 532 nm excitation laser. Selected-area electron diffraction (SAED) patterns were taken with a JEM-ARM200F (JEOL). STEM observations were performed using a Titan G2 Cubed instrument (TFS Inc.) operated at 300 kV. The EEL spectra were obtained using a Quantum spectrometer (Gatan Inc.) with monochromatic excitation to attain an energy resolution of 0.25 eV. The probe-forming semiangle was set to 21.4 mrad for STEM observations. Annular dark-field (ADF) STEM images were recorded in the detection angle range of 38–184 mrad. Probe currents of 15 and 45 pA were used for STEM and EELS measurements, respectively. Spectrum imaging measurements were performed simultaneously at the Ti $L_{2,3}$- and O K-edges in 0.35–0.50 nm steps for an integration time of 0.3 s around Pt nanoparticles from the plan-view direction. For EELS measurements, we focused on Pt nanoparticles with a diameter of 1.7–3.4 nm. No sample drift attributable to charge-up was observed during the STEM-EELS measurements, probably because the slight presence of oxygen vacancies on the TiO_2 surface allowed charge dissipation. The measured region remained essentially unchanged after the STEM-EELS measurements. In addition, the EELS measurements were conducted under a slightly defocused condition to minimize possible beam damage. XPS was performed using an AXIS-ULTRA spectrometer (Shimadzu) equipped with an Al X-ray source. All samples were measured under identical charge-neutralization conditions on insulating tape. The peak shift derived from the charge build-up in catalysts was corrected by adjusting the binding energy of the Ti 2p peak to 458.8 eV.[42,43] All XPS spectra were fitted using Gaussian–Lorentzian symmetric peak shapes and an iterative Shirley background.[44] Scanning electron microscopy (SEM) images were captured using a Helios Hydra CX microscope (TFS Inc.). Electron paramagnetic resonance (EPR) data were taken with a JEOL JES-FA200 spectrometer operating near 9.444 GHz.

First-principles calculations

We performed first-principles calculations based on the DFT using projector-augmented wave potentials as implemented in the Vienna *Ab initio* Simulation Package (VASP) code.[45,46] The generalized gradient approximation with the PBEsol parameterization was used to describe the exchange correlation,[47] and the Dudarev "+U" term[48] was added for Ti 3d states. We set the value of U to 4.2 eV, following previous reports.[36] Spin-polarized calculations were performed at a plane-wave cutoff energy of 520 eV. Slab models with {101} surfaces were constructed after optimizing the structure of the TiO_2 unit cell. A Pt34 nanoparticle was put on the one of the {101} surface of TiO_2 slab models so that the {101} plane of Pt was parallel to the surface and the center of the nanoparticle was just above one of the oxygen atoms on the surface of TiO_2. Note that the Pt34 nanoparticle was prepared using the lattice parameters of an optimized Pt unit cell. The in-plane sizes and thicknesses of slab models were set to 21.9 Å × 18.3 Å × 10.1 Å for {101} surfaces. The vacuum space above the slab was 15 Å thick. All atoms in the cell were relaxed, except for those in the bottom three atomic layers, which were fixed in their bulk positions. Electronic energies converged to 10^{-4} eV, and ionic relaxations were considered to converge when the forces on ions were less than 0.02 eV $Å^{-1}$. k-Point meshes were calculated by VASP using a k-spacing of 0.5 $Å^{-1}$. A dipole correction to surface models was included in the normal direction of the surface. The formation energies of oxygen vacancies for Pt/TiO_2 and TiO_2 slabs were calculated using the total energies for the corresponding slabs with and without oxygen vacancies and the energy of a gas-phase oxygen molecule. Neutral oxygen vacancies were considered for simplicity. Atomic charges were estimated using Bader's analysis[49] based on the numerical implementation developed by Henkelman *et al.*[50]

Results and discussion

Fig. 1(a) presents a schematic illustration of the thin-film-based Pt/TiO_2 model catalyst. The out-of-plane XRD pattern of the TiO_2 film on the r-plane Al_2O_3 substrate is shown in Fig. 1(b). According to the literature, (101)-oriented rutile-type TiO_2 can be stabilized on r-Al_2O_3.[40] The calculated out-of-plane lattice constant of the TiO_2 film is 2.48 Å. This value is in good agreement with the (101) lattice spacing of the rutile-type TiO_2 powder, indicating that a fully relaxed and stoichiometric TiO_2 film was obtained. The sheet resistance of the TiO_2 film before Pt deposition exceeded the measurement limit of our multimeter (~1 MΩ). The crystal structure of TiO_2 was confirmed to be rutile-type using Raman spectroscopy (Fig. S1),[51] and the SAED pattern at the TiO_2/Al_2O_3 interface further confirmed that a (101)-oriented rutile-type TiO_2 film was epitaxially grown on the r-plane Al_2O_3 substrate (Fig. S2). The epitaxial relationship is TiO_2 (101)[100]//Al_2O_3(1$\bar{1}$02)[0001]. The surface structure of the TiO_2 thin film was studied by AFM and cross-sectional STEM (Fig. 1(c) and (d)). These results confirm that the TiO_2 film is relatively flat with a thickness of ~170 nm. After processing the TiO_2 film into thin foil for plan-view ADF-STEM, Pt nanoparticles were loaded *via* the photoreduction method. The plan-view ADF-STEM image of the TiO_2 (101) thin film after the deposition of Pt nanoparticles is shown in Fig. 1(e), in which the bright particles are composed of Pt, as confirmed by energy-dispersive X-ray spectroscopy (EDS; Fig. S3). The contrast of the ADF-STEM image depends on the atomic number (Z) of the constituent element, and elements with larger Z values show higher contrasts.[52] Consequently, Pt (Z = 78) nanoparticles are brighter than TiO_2 particles (Z = 22 and 16 for Ti and O) in Fig. 1(e). Fig. 1(e) also shows that Pt nanoparticles are well dispersed on TiO_2 with no noticeable agglomeration.

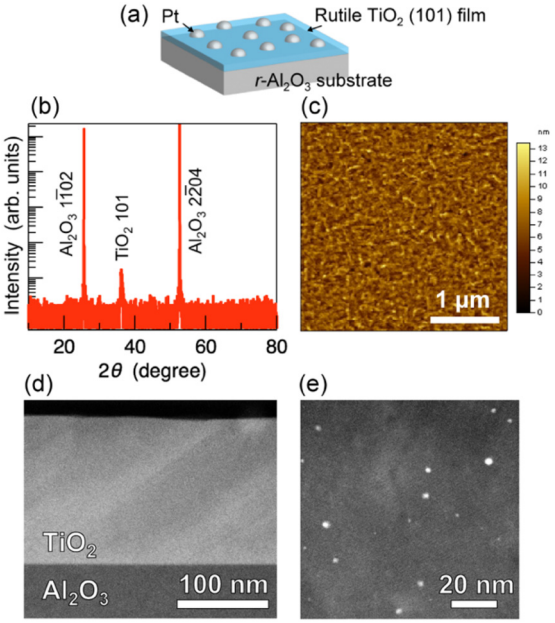

Fig. 1 (a) Schematic illustration of the thin-film-based Pt/TiO_2 model catalyst. (b) Out-of-plane XRD pattern, (c) AFM image, and (d) cross-sectional ADF-STEM image of the TiO_2 (101) thin film. (e) Plan-view ADF-STEM image of the TiO_2 (101) thin film after the deposition of Pt nanoparticles.

EELS was performed at the O K- and Ti $L_{2,3}$-edges to determine the local electronic structure of TiO_2 around Pt nanoparticles. As shown in Fig. 2(a), the EEL spectra of the sample were obtained from two regions: one is directly below Pt nanoparticles and the other is around Pt nanoparticles. Because the difference in the EEL spectra of these two regions is clearer at the O K-edge, most probably because the O K-edge spectrum is sensitive to local asymmetry and ligands,[53,54] only the EEL spectrum measured at the O K-edge is shown in Fig. 2(b). The EEL spectrum at the Ti–$L_{2,3}$ edge is shown in Fig. S4, where no clear change in the spectrum is observed. It is known that two peaks are observed at approximately 532 and 533 eV in the EEL spectrum of TiO_2 at O K-edge.[55] These two peaks correspond to the unoccupied O p state that hybridizes with the t_{2g} and e_g orbitals of Ti 3d, respectively.[55,56] It is well known that the intensity of the t_{2g} peak is lower in the EEL spectrum of Ti_2O_3 than in that of TiO_2 due to the presence of electrons in the t_{2g} orbital.[53,57] This change in the EEL spectra at the O

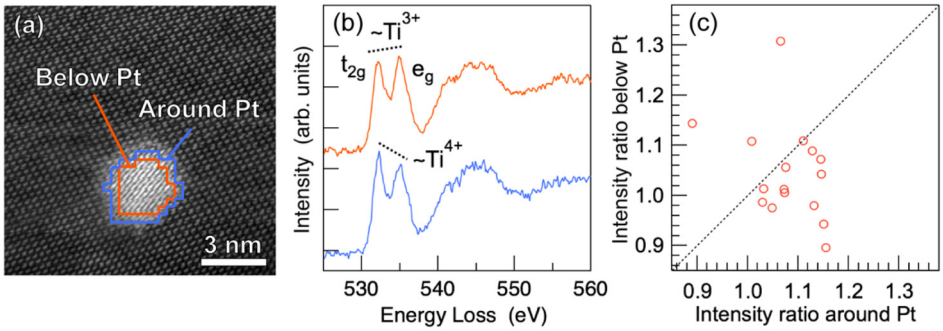

Fig. 2 ADF-STEM image of a Pt nanoparticle on TiO_2 (101) and schematic illustrations in blue and orange that show regions where STEM-EELS was performed. (b) O K-edge EEL spectra measured from both areas in (a). (c) Intensity ratios of the t_{2g}/e_g peaks in the O K-edge EEL spectra below and around Pt nanoparticles.

K-edge is also observed for other Ti-containing materials with and without oxygen vacancies.[57,58] It suggests that the valence state of Ti is close to +4 in the region around Pt but close to +3 in the region directly below Pt. For further analysis, the intensity ratio t_{2g}/e_g of the two peaks was defined and calculated from the height of each peak. As discussed above, the intensity ratio of Ti^{3+} is expected to be smaller than that of Ti^{4+}. Indeed, we found that the intensity ratios t_{2g}/e_g are 0.94 for the spectrum measured directly below Pt and 1.15 for the spectrum measured around Pt (Fig. 2(b)). The EEL spectra may contain contributions from the surface and back-surface of the TEM foil, and compared with the bulk region, the surface regions will contain more oxygen vacancies and Ti atoms in the Ti^{3+} state because the oxygen vacancy formation energy at the surface is generally lower than that in the bulk region.[36] Therefore, the EEL spectrum of the sample can vary depending on the local thickness of the TEM foil. To reduce the effect of the sample thickness on the EEL spectrum and to obtain more systematic information, EELS of 15 Pt nanoparticles at different locations on the TEM foil was performed, and the O K-edge intensity ratios t_{2g}/e_g are plotted in Fig. 2(c). For each nanoparticle, the spectra below and around Pt were acquired from the same local area of TiO_2, ensuring comparable thickness. In Fig. 2(c), the vertical axis is the intensity ratio of the O K-edge directly below Pt and the horizontal axis is the intensity ratio of the area around Pt. Therefore, the dotted line would indicate that the intensity ratios are the same in regions directly below Pt and around Pt. Because most of the markers exist below the dotted line, we can conclude that the valence state of Ti is closer to +3 directly below Pt than in the area around Pt. Notably, this result does not mean that Ti^{3+} ions do not exist at the Pt–TiO_2 perimeter, as they are often reported to be the active sites of supported metal catalysts. Because EELS was performed from the plan-view direction, a subtle change in the amount of Ti^{3+} around Pt nanoparticles at the surface may be buried in the information from the bulk region of the sample. In this regard, these results suggest that a substantial amount of oxygen vacancies is present directly below Pt.

XPS was used to study the electronic structure of Pt on TiO_2 (Fig. 3(a)). Two model Pt/TiO_2 catalysts with different Pt loadings were analyzed. The Pt loading of one sample was the same as that of the sample used for STEM-EELS, whereas the Pt loading of the second sample was 10 times higher. The samples were named Pt(TEM)–TiO_2 and Pt(×10)–TiO_2, respectively. Notably, the intensity of the Pt 4f XPS signal is ~10 times stronger for Pt(×10)–TiO_2 than Pt–TiO_2 as is evident from the signal-to-noise (S/N) ratio of their spectra. In the Pt 4f XPS spectra of Pt–TiO_2 and Pt(×10)–TiO_2, the Pt $4f_{7/2}$ and $4f_{5/2}$ peaks are observed at 70.8 eV, 74.2 eV and 71.3 eV, 74.6 eV, respectively. The binding energies of peaks in the XPS spectrum of Pt(TEM)–TiO_2 are in the range of those reported for negatively charged Pt, indicating that Pt nanoparticles on TiO_2 (101) are present in the $Pt^{\delta-}$ state. By contrast, the binding energies in the XPS spectrum of Pt(×10)–TiO_2 are close to those reported for metallic Pt; hence, we can assume that Pt in Pt(×10)–TiO_2 is metallic. SEM observations revealed that Pt exists as nanoparticles in the Pt(TEM)–TiO_2 sample (Fig. 3(b)); hence, the effect of charge transfer manifests itself. Note: some of the nanoparticles seem much larger than those observed using STEM (Fig. 1(d)), but we confirmed that larger nanoparticles are composed of nanoparticles with a size of a

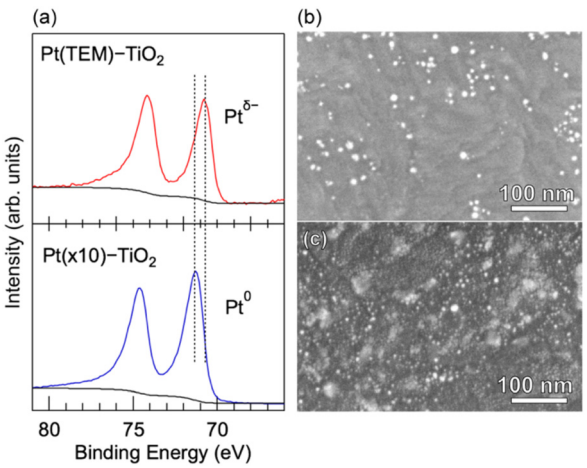

Fig. 3 (a) Pt 4f XPS spectra of Pt(TEM)–TiO_2 and Pt(×10)–TiO_2 samples. SEM images of (b) Pt(TEM)–TiO_2 and (c) Pt(×10)–TiO_2 samples.

few nanometers, *i.e.*, they are agglomerations of small nanoparticles (Fig. S5). On the other hand, Pt is deposited as film-like aggregations of Pt nanoparticles on the Pt(×10)–TiO_2 sample, as shown in Fig. 3(c). Assuming that the amount of charge transfer is finite, as is reported for Pt/CeO_2,[59] the change in the charge state of Pt due to possible charge transfer can be buried and go unnoticed in the case of Pt(×10)–TiO_2 and the bulk properties of Pt will be observed. Several studies on the stabilization of the $Pt^{\delta-}$ state on TiO_2 based on the XPS spectrum of powder Pt/TiO_2 catalysts have been published.[60–64] The $Pt^{\delta-}$ state is generally explained in terms of so-called strong metal–support interaction (SMSI): charge transfer from TiO_x which is partly covering Pt. Although we cannot completely rule out the possibility that the $Pt^{\delta-}$ state observed herein comes from SMSI, it is less likely because we found no evidence of apparent SMSI in Pt/TiO_2 catalysts that underwent the same postdeposition treatment.[17,41] Therefore, we can conclude that the direct charge transfer from the TiO_2 support to Pt due to the metal–support interaction between Pt and TiO_2 (101) is the origin of the $Pt^{\delta-}$ state. Only a Ti^{4+} component was observed in the Ti 2p spectra for both samples (Fig. S6). This is most probably because Ti^{3+} mainly exists below Pt nanoparticles, and hence the signal of Ti^{3+} is too small to be detected by XPS. It should be noted that small Pt nanoparticles are known to exhibit positive binding-energy shifts due to reduced screening of the photoemission final state.[65–67] However, in our system, the smaller Pt nanoparticles in Pt (TEM)–TiO_2 show a negative BE shift relative to bulk-like (film-like) Pt, which is opposite to the typical size-dependent trend. This suggests that the observed binding-energy shift originates predominantly from an initial-state effect, *i.e.*, charge transfer from TiO_2 to Pt, rather than from differences in final-state screening. Possible morphology-related effects, such as differential charging, can also be excluded because both samples were measured under identical charge-neutralization conditions on insulating tape. We have performed EPR measurements to further investigate the presence of Ti^{3+} species for Pt (TEM)–TiO_2 and Pt(×10)–TiO_2 samples at room temperature in two configurations, where the magnetic field was applied parallel and perpendicular to the TiO_2 (101) plane. However, no signal assignable to Ti^{3+} ($g \approx 1.9$–2.0, expected at 340–355 mT) was observed (Fig. S7). This result indicates that the amount of Ti^{3+} species is below the detection limit of EPR.

To further investigate the interaction between Pt and TiO_2, we performed DFT calculations. As shown in Fig. 4(a), a slab model of TiO_2 with an exposed (101) surface was fabricated and a Pt nanoparticle composed of 34 Pt atoms was placed on it. The projection view of the Pt–TiO_2 interface containing the bottom layer of Pt nanoparticles and the top two layers of O and Ti is shown in Fig. 4(a), bottom. We calculated the oxygen vacancy formation energy and the charge state of Pt nanoparticles using Bader charge analysis. Because the formation energies of oxygen vacancies and the Bader charge of Pt nanoparticles can vary depending on the location of oxygen vacancies with respect to Pt nanoparticles, we considered every oxygen ion on the outermost layer of the slab. The calculated oxygen vacancy formation energies on the TiO_2 surface and the Bader charge of Pt are plotted in Fig. 4(b) and (c) as a function of the in-plane distance between the center of the Pt nanoparticle and the oxygen atom of interest. Two-dimensional distributions of these parameters are shown in Fig. S8. The oxygen vacancy formation energy in the absence of Pt is 4.14 eV. This energy drastically decreases to 1.86 eV below the Pt nanoparticle. Therefore, the oxygen vacancy formation energy is the lowest directly below Pt. It increases concentrically as the location of the oxygen vacancy moves outward, approaching the value of the bare TiO_2 surface. These results are consistent with EELS results, which demonstrate that more Ti^{3+} ions are present below Pt nanoparticles because electrons afforded by the introduction of oxygen vacancies reduce Ti^{4+} ions in TiO_2 to Ti^{3+}. Notably, the formation of oxygen vacancies near Pt can generally be explained using the hydro-

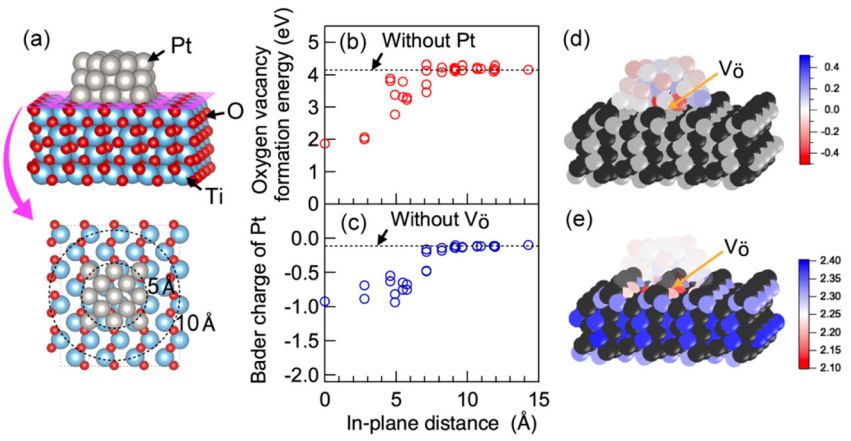

Fig. 4 (a) Graphical illustration of the Pt/TiO_2 (101) slab model used for DFT calculations. The bottom panel in (a) shows the atomic arrangement near the interface. (b) Oxygen vacancy formation energy and (c) Bader charge of Pt as a function of the lateral distance between the center of Pt nanoparticle and the location of oxygen vacancies. Distribution of charges (d) on a Pt nanoparticle and (e) Ti in TiO_2 when oxygen vacancies are present under the Pt nanoparticle. The Pt nanoparticle in (e) is rendered semi-transparent to enhance the visibility of Ti.

gen spillover mechanism,[68,69] in which hydrogen atoms created by the dissociative chemisorption of H_2 molecules on Pt nanoparticles migrate to the TiO_2 surface and reduce TiO_2 surfaces to TiO_{2-x} during postdeposition treatment. In this regard, our calculations demonstrate that the oxygen vacancy formation energy at the Pt–TiO_2 interface is lower compared to that on the bare TiO_2 surface, facilitating the interaction between the possible hydrogen atom and lattice oxygen at the Pt–TiO_2 interface. Another possibility is that Pt nanoparticles grow selectively on the possible native defect sites on the as-prepared TiO_2 surface because oxygen vacancies are energetically favorable sites for Pt atom adsorption.[70–72] Indeed, we observed many line contrasts that correspond to stacking faults on the TiO_2 surface (Fig. S9), where more oxygen vacancies can exist due to lattice strain.[73] However, because we found no indication that Pt nanoparticles selectively grow on such defect sites, the latter possibility is less likely.

As shown in Fig. 4(c), the Bader charge of Pt nanoparticles in the absence of oxygen vacancies is negative ($-0.115|e|$), indicating that the $Pt^{\delta-}$ state is stable. The presence of oxygen vacancies promotes charge transfer to Pt nanoparticles, and Pt becomes more negatively charged. The charge distributions on Pt nanoparticles and the support when an oxygen vacancy is formed under the center of the Pt nanoparticle are shown in Fig. 4(d) and (e). Results show that Pt and Ti atoms near oxygen vacancies are more negatively charged than other atoms. This behavior can be explained as follows: when a neutral oxygen vacancy is formed at the Pt–TiO_2 interface, Pt and Ti atoms can receive electrons donated by the oxygen atom forming the oxygen vacancy. Consequently, Ti becomes trivalent and Pt nanoparticles become $Pt^{\delta-}$. Because Pt is more electronegative than Ti (Pauling's electronegativities of Pt and Ti are 2.28 and 1.44, respectively), it can be assumed that Pt atoms accept more electrons than Ti atoms and entire Pt nanoparticles become negatively charged. DFT calculations indicate that the interaction between Pt nanoparticles and the support facilitates the formation of oxygen vacancies in TiO_2 and the charge transfer from TiO_2 to Pt. Importantly, this study demonstrates that the $Pt^{\delta-}$ state can be stabilized without inducing the SMSI state, which is often considered the origin of the $Pt^{\delta-}$ state.[60,62,63] We note that several mechanistic points discussed above are primarily supported by DFT calculations. While these results provide useful insight, the experimental evidence remains indirect or limited, and the interpretations should therefore be considered indicative rather than definitive. Cross-sectional STEM–EELS observations could directly confirm that oxygen vacancies are located beneath the Pt nanoparticles. While such measurements could also provide direct evidence regarding the presence of SMSI and/or oxygen on the Pt surface, they are technically challenging and are therefore left for future work.

Conclusions

Herein, a model Pt/TiO_2 catalyst based on an epitaxial TiO_2 thin film was developed and the distribution of Ti^{3+} ions and the charge state of Pt nanoparticles were investigated in detail. STEM-EELS measurements at the O K-edge revealed that oxygen vacancies were easily formed just below Pt, which was consistent with DFT calculations. XPS measurements and Bader charge analysis indicated that Pt nanoparticles on TiO_2 (101) were negatively charged, and the presence of oxygen vacancies promoted the charge transfer from TiO_2 to Pt. This study demonstrated that the charge state of Pt, which plays a crucial role in the catalytic activity of supported metal catalysts, can be tuned using the stoichiometry of the support, providing an important guideline for controlling metal–support interactions to develop catalysts with desired properties.

Conflicts of interest

There are no conflicts to declare.

Data availability

The data supporting this article have been uploaded as part of the supplementary information (SI). Supplementary information: Raman spectrum of the TiO_2 film, SAED pattern at the TiO_2/Al_2O_3 interface, Pt EDS map, EEL spectra of Ti $L_{2,3}$-edge directly below Pt and around Pt, SEM image of the Pt(TEM)–TiO_2, XPS spectra of Ti 2p, EPR spectra of Pt(TEM)–TiO_2 and Pt(×10)–TiO_2, the atomic arrangement near the interface showing the distribution of oxygen vacancy formation energies and Pt charge states upon the formation of oxygen vacancies based on DFT calculations, ADF-STEM image of TiO_2 film. See DOI: https://doi.org/10.1039/d5nr02953h.

Acknowledgements

This study was supported by the Japan Science and Technology Agency (JST) FOREST project (Grant Number JPMJFR201UA); JSPS KAKENHI (Grant No. 23H02046); Asahi Glass Foundation. A part of this work was supported by "Advanced Research Infrastructure for Materials and Nanotechnology in Japan (ARIM)" of the Ministry of Education, Culture, Sports, Science and Technology (MEXT). Proposal Number JPMXP1223KU1028.

References

1 M. Boudart, *Adv. Catal.*, 1969, **20**, 153–166.
2 L. C. Liu and A. Corma, *Chem. Rev.*, 2018, **118**, 4981–5079.
3 T. W. van Deelen, C. H. Mejia and K. P. de Jong, *Nat. Catal.*, 2019, **2**, 955–970.
4 M. Cargnello, V. V. T. Doan-Nguyen, T. R. Gordon, R. E. Diaz, E. A. Stach, R. J. Gorte, P. Fornasiero and C. B. Murray, *Science*, 2013, **341**, 771–773.
5 I. X. Green, W. J. Tang, M. Neurock and J. T. Yates, *Science*, 2011, **333**, 736–739.

6 A. R. Puigdollers, P. Schlexer, S. Tosoni and G. Pacchioni, *ACS Catal.*, 2017, **7**, 6493–6513.
7 D. Widmann and R. J. Behm, *Acc. Chem. Res.*, 2014, **47**, 740–749.
8 L. Li and X. C. Zeng, *J. Am. Chem. Soc.*, 2014, **136**, 15857–15860.
9 Y. Maeda, Y. Iizuka and M. Kohyama, *J. Am. Chem. Soc.*, 2013, **135**, 906–909.
10 P. Schlexer, D. Widmann, R. J. Behm and G. Pacchioni, *ACS Catal.*, 2018, **8**, 6513–6525.
11 Y. G. Wang, D. C. Cantu, M. S. Lee, J. Li, V. A. Glezakou and R. Rousseau, *J. Am. Chem. Soc.*, 2016, **138**, 10467–10476.
12 H. V. Thang and G. Pacchioni, *Catal. Lett.*, 2019, **149**, 390–398.
13 S. Oh, H. Ha, H. Choi, C. Jo, J. Cho, H. Choi, R. Ryoo, H. Y. Kim and J. Y. Park, *J. Chem. Phys.*, 2019, **151**, 234716.
14 K. G. Azzam, I. V. Babich, K. Seshan and L. Lefferts, *J. Catal.*, 2007, **251**, 153–162.
15 S. S. Kim, H. H. Lee and S. C. Hong, *Appl. Catal., A*, 2012, **423**, 100–107.
16 C. M. Kalamaras, P. Panagiotopoulou, D. I. Kondarides and A. M. Efstathiou, *J. Catal.*, 2009, **264**, 117–129.
17 R. Aso, H. Hojo, Y. Takahashi, T. Akashi, Y. Midoh, F. Ichihashi, H. Nakajima, T. Tamaoka, K. Yubuta, H. Nakanishi, H. Einaga, T. Tanigaki, H. Shinada and Y. Murakami, *Science*, 2022, **378**, 202–206.
18 T. Luttrell, S. Halpegamage, E. Sutter and M. Batzill, *Thin Solid Films*, 2014, **564**, 146–155.
19 A. Bruix, J. A. Rodriguez, P. J. Ramirez, S. D. Senanayake, J. Evans, J. B. Park, D. Stacchiola, P. Liu, J. Hrbek and F. Illas, *J. Am. Chem. Soc.*, 2012, **134**, 8968–8974.
20 C. T. Campbell, *Nat. Chem.*, 2012, **4**, 597–598.
21 G. Pacchioni, *Phys. Chem. Chem. Phys.*, 2013, **15**, 1737–1757.
22 Y. G. Wang, Y. Yoon, V. A. Glezakou, J. Li and R. Rousseau, *J. Am. Chem. Soc.*, 2013, **135**, 10673–10683.
23 Y. W. Chung, W. J. Lo and G. A. Somorjai, *Surf. Sci.*, 1977, **64**, 588–602.
24 U. Diebold, *Surf. Sci. Rep.*, 2003, **48**, 53–229.
25 S. Y. Huang, P. Ganesan, S. Park and B. N. Popov, *J. Am. Chem. Soc.*, 2009, **131**, 13898.
26 K. M. Naik, E. Higuchi and H. Inoue, *Nanoscale*, 2020, **12**, 11055–11062.
27 K. M. Naik, E. Higuchi and H. Inoue, *J. Power Sources*, 2020, **455**, 227972.
28 B. Kraeutler and A. J. Bard, *J. Am. Chem. Soc.*, 1978, **100**, 5985–5992.
29 C. R. Henry, *Surf. Sci. Rep.*, 1998, **31**, 235–325.
30 S. L. Chen, F. Xiong and W. X. Huang, *Surf. Sci. Rep.*, 2019, **74**, 100471.
31 A. Sasahara, C. L. Pang and H. Onishi, *J. Phys. Chem. B*, 2006, **110**, 13453–13457.
32 Y. Watanabe, X. Y. Wu, H. Hirata and N. Isomura, *Catal. Sci. Technol.*, 2011, **1**, 1490–1495.
33 S. Bonanni, K. Aït-Mansour, H. Brune and W. Harbich, *ACS Catal.*, 2011, **1**, 385–389.
34 S. Bonanni, K. Aït-Mansour, W. Harbich and H. Brune, *J. Am. Chem. Soc.*, 2012, **134**, 3445–3450.
35 S. Bonanni, K. Aït-Mansour, W. Harbich and H. Brune, *J. Am. Chem. Soc.*, 2014, **136**, 8702–8707.
36 B. J. Morgan and G. W. Watson, *J. Phys. Chem. C*, 2009, **113**, 7322–7328.
37 H. Perron, C. Domain, J. Roques, R. Drot, E. Simoni and H. Catalette, *Theor. Chem. Acc.*, 2007, **117**, 565–574.
38 K. D. Schierbaum, S. Fischer, M. C. Torquemada, J. L. deSegovia, E. Roman and J. A. MartinGago, *Surf. Sci.*, 1996, **345**, 261–273.
39 Y. W. Chung and W. B. Weissbard, *Phys. Rev. B:Condens. Matter Mater. Phys.*, 1979, **20**, 3456–3461.
40 Y. Matsumoto, R. Takahashi, M. Murakami, T. Koida, X. J. Fan, T. Hasegawa, T. Fukumura, M. Kawasaki, S. Y. Koshihara and H. Koinuma, *Jpn. J. Appl. Phys.*, 2001, **40**, L1204–L1206.
41 H. Hojo, M. Gondo, S. Yoshizaki and H. Einaga, *Nano Lett.*, 2022, **22**, 145–150.
42 E. I. Vovk, A. V. Kalinkin, M. Y. Smirnov, I. O. Klembovskii and V. I. Bukhtiyarov, *J. Phys. Chem. C*, 2017, **121**, 17297–17304.
43 J. S. Lee and W. Y. Choi, *J. Phys. Chem. B*, 2005, **109**, 7399–7406.
44 K. Taira and H. Einaga, *Catal. Lett.*, 2019, **149**, 965–973.
45 P. E. Blochl, *Phys. Rev. B:Condens. Matter Mater. Phys.*, 1994, **50**, 17953–17979.
46 G. Kresse and J. Furthmuller, *Phys. Rev. B:Condens. Matter Mater. Phys.*, 1996, **54**, 11169–11186.
47 J. P. Perdew, A. Ruzsinszky, G. I. Csonka, O. A. Vydrov, G. E. Scuseria, L. A. Constantin, X. L. Zhou and K. Burke, *Phys. Rev. Lett.*, 2008, **100**, 136406.
48 S. L. Dudarev, G. A. Botton, S. Y. Savrasov, C. J. Humphreys and A. P. Sutton, *Phys. Rev. B:Condens. Matter Mater. Phys.*, 1998, **57**, 1505–1509.
49 R. F. W. Bader, *Acc. Chem. Res.*, 1985, **18**, 9–15.
50 G. Henkelman, A. Arnaldsson and H. Jonsson, *Comput. Mater. Sci.*, 2006, **36**, 354–360.
51 T. Mazza, E. Barborini, P. Piseri, P. Milani, D. Cattaneo, A. Li Bassi, C. E. Bottani and C. Ducati, *Phys. Rev. B: Condens. Matter Mater. Phys.*, 2007, **75**, 045416.
52 S. J. Pennycook and D. E. Jesson, *Phys. Rev. Lett.*, 1990, **64**, 938–941.
53 V. S. Lusvardi, M. A. Barteau, J. G. Chen, J. Eng, B. Fruhberger and A. Teplyakov, *Surf. Sci.*, 1998, **397**, 237–250.
54 L. Soriano, M. Abbate, J. Vogel, J. C. Fuggle, A. Fernandez, A. R. Gonzalezelipe, M. Sacchi and J. M. Sanz, *Surf. Sci.*, 1993, **290**, 427–435.
55 S. Räth, F. Gracia, F. Yubero, J. P. Holgado, A. I. Martin, D. Batchelor and A. R. González-Elipe, *Nucl. Instrum. Methods Phys. Res., Sect. B*, 2003, **200**, 248–254.
56 S. C. Ray, D. K. Mishra, A. B. Panda, H. T. Wang, S. Bhattacharya and W. F. Pong, *J. Phys. Chem. C*, 2022, **126**, 8947–8952.
57 M. K. Tian, M. Mahjouri-Samani, G. Eres, R. Sachan, M. Yoon, M. F. Chisholm, K. Wang, A. A. Puretzky,

C. M. Rouleau, D. B. Geohegan and G. Duscher, *ACS Nano*, 2015, **9**, 10482–10488.
58 Z. H. Ren, L. Y. Ruan, L. C. Yin, K. Akkiraju, L. Giordano, Z. R. Liu, S. Li, Z. X. Ye, S. D. Li, H. S. Yang, Y. Wang, H. Tian, G. Liu, Y. Shao-Horn and G. R. Han, *Adv. Mater.*, 2022, **34**, 2202072.
59 Y. Lykhach, S. M. Kozlov, T. Skala, A. Tovt, V. Stetsovych, N. Tsud, F. Dvorak, V. Johanek, A. Neitzel, J. Myslivecek, S. Fabris, V. Matolin, K. M. Neyman and J. Libuda, *Nat. Mater.*, 2016, **15**, 284.
60 J. Ohyama, A. Yamamoto, K. Teramura, T. Shishido and T. Tanaka, *ACS Catal.*, 2011, **1**, 187–192.
61 F. Long, X. C. Cao, P. Liu, X. Jiang, J. C. Jiang, X. L. Zhang and J. M. Xu, *J. Cleaner Prod.*, 2022, **375**, 133975.
62 H. B. Huang, D. Y. C. Leung and D. Q. Ye, *J. Mater. Chem.*, 2011, **21**, 9647–9652.
63 J. Fu, X. Zhang, H. Li, B. Chen, S. Ye, N. Zhang, Z. Yu, J. Zheng and B. Chen, *J. Hazard. Mater.*, 2022, **426**, 128088.
64 J. C. Colmenares, A. Magdziarz, M. A. Aramendia, A. Marinas, J. M. Marinas, F. J. Urbano and J. A. Navio, *Catal. Commun.*, 2011, **16**, 1–6.
65 Z. Bayindir, P. N. Duchesne, S. C. Cook, M. A. MacDonald and P. Zhang, *J. Chem. Phys.*, 2009, **131**, 244716.
66 Y. Watanabe, X. Y. Wu, H. Hirata and N. Isomura, *Catal. Sci. Technol.*, 2011, **1**, 1490–1495.
67 R. Siburian, A. M. Ali, K. Sebayang, M. Supeno, K. Tarigan, C. Simanjuntak, S. P. Aritonang and F. Hutagalung, *Sci. Rep.*, 2021, **11**, 2532.
68 R. Prins, *Chem. Rev.*, 2012, **112**, 2714–2738.
69 W. Karim, C. Spreafico, A. Kleibert, J. Gobrecht, J. VandeVondele, Y. Ekinci and J. A. van Bokhoven, *Nature*, 2017, **541**, 68–71.
70 H. Iddir, V. Skavysh, S. Ögüt, N. D. Browning and M. M. Disko, *Phys. Rev. B:Condens. Matter Mater. Phys.*, 2006, **73**, 041403.
71 V. Çelik, H. Ünal, E. Mete and S. Ellialtioglu, *Phys. Rev. B: Condens. Matter Mater. Phys.*, 2010, **82**, 205113.
72 T. Y. Chang, Y. Tanaka, R. Ishikawa, K. Toyoura, K. Matsunaga, Y. Ikuhara and N. Shibata, *Nano Lett.*, 2014, **14**, 134–138.
73 B. Feng, I. Sugiyama, H. Hojo, H. Ohta, N. Shibata and Y. Ikuhara, *Sci. Rep.*, 2016, **6**, 20288.